Electronic Supplementary Material (ESI) for Sustainable Energy & Fuels.

Support information for

Switching Charge Kinetic from type-I to Z-Scheme of g-C_3N_4 and $ZnIn_2S_4$ by Defective Engineering for Efficient and Durable Hydrogen Evolution

Mingya Wang†, Shushu Huang†, Xin Pang, Meiting Song, Chunfang Du* and Yiguo Su*

Inner Mongolia Key Laboratory of Chemistry and Physics of Rare Earth Materials, School of Chemistry and Chemical Engineering, Inner Mongolia University, Hohhot, Inner Mongolia 010021, PR China

†Mingya Wang and Shushu Huang contributed equally to this work.

Corresponding author. Tel: +86-471-4344579. E-mail address: cesyg@imu.edu.cn (Y. Su). cedchf@imu.edu.cn (C. Du)

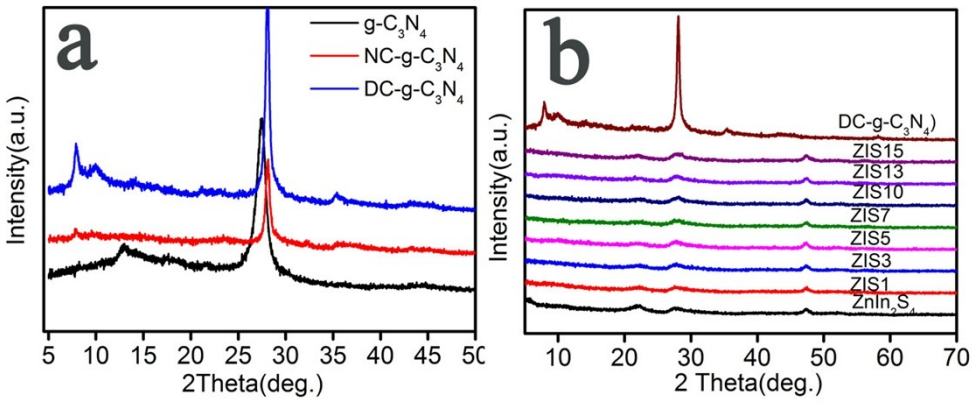

Fig. S1 XRD patterns of g-C_3N_4, NC-g-C_3N_4 and DC-g-C_3N_4 (a). XRD patterns of DC-g-C_3N_4, $ZnIn_2S_4$, and DC-g-C_3N_4/$ZnIn_2S_4$ heterojunctions with different DC-g-C_3N_4 loading content.

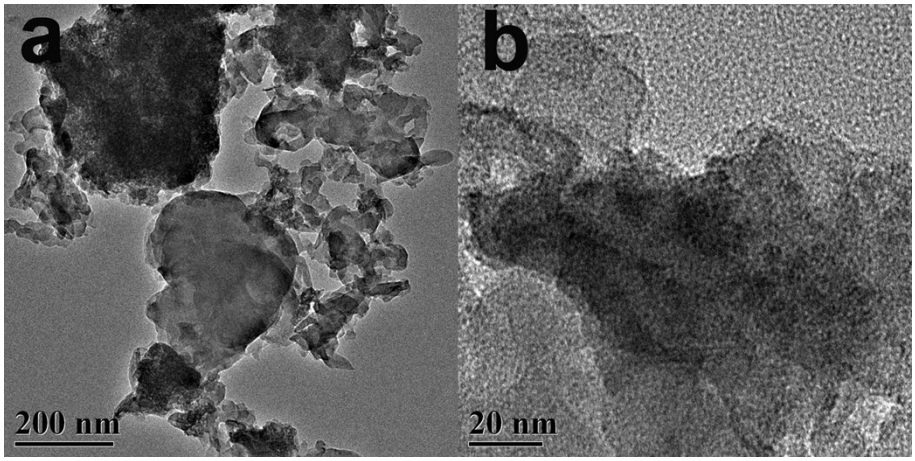

Fig. S2 TEM images of g-C_3N_4.

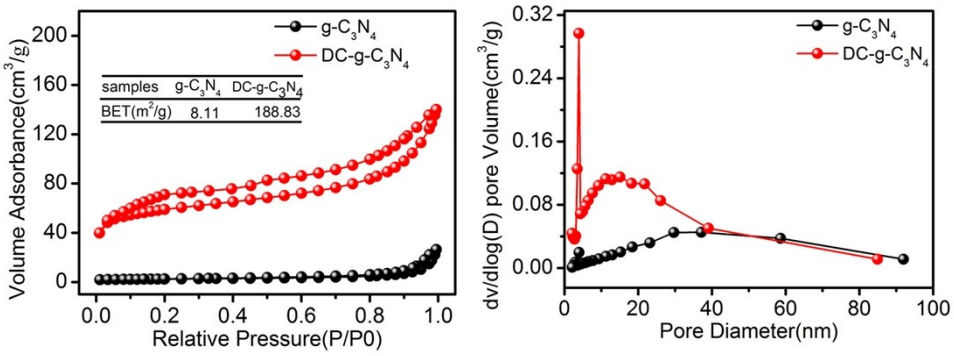

Fig. S3 N_2 adsorption-desorption isotherms (a) and the corresponding pore size distribution curves (b) of g-C_3N_4 and DC- g-C_3N_4.

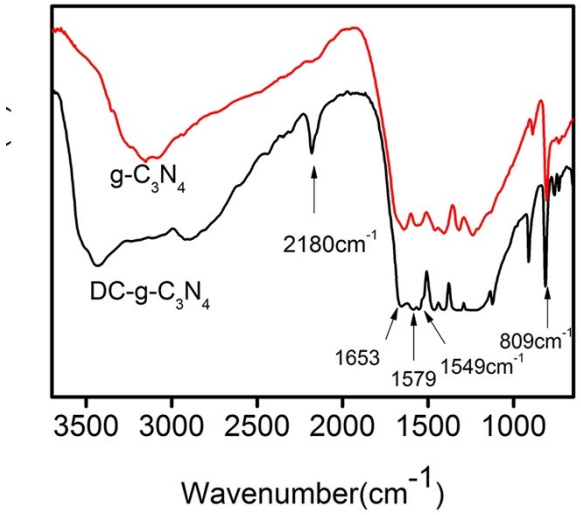

Fig. S4 FT-IR spectra of g-C_3N_4 and DC-g-C_3N_4.

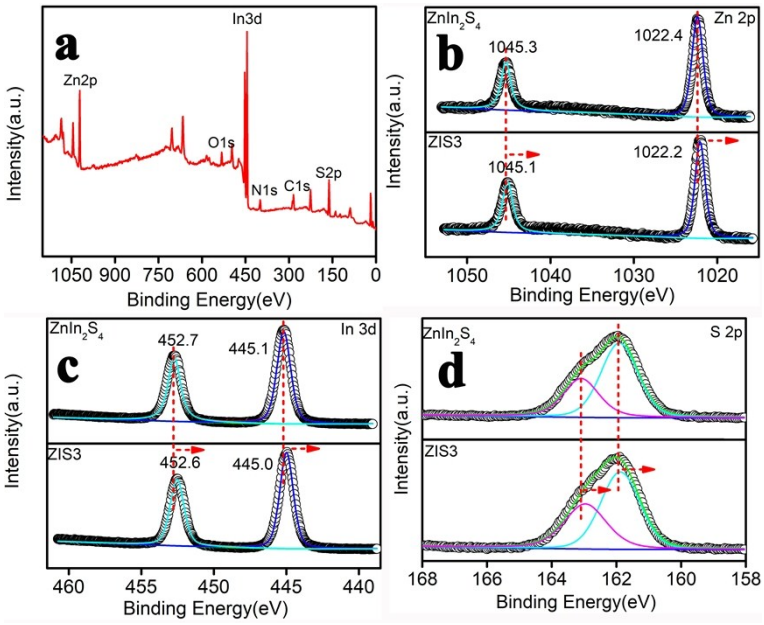

Fig. S5 XPS spectra: the survey spectrum of ZIS3 (a), Zn 2p orbital, (b) In 3d orbital (c) and S 2p orbital (d), respectively.

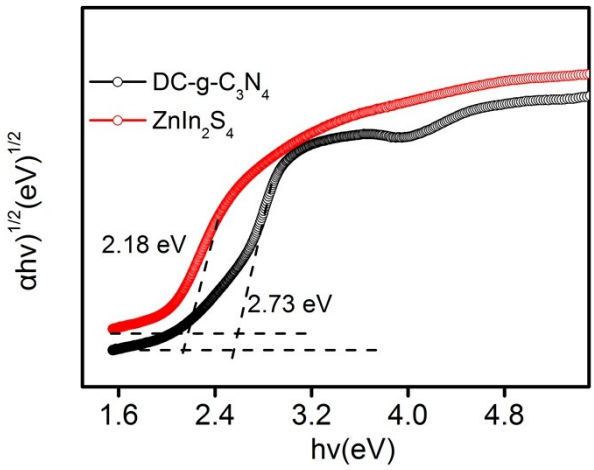

Fig. S6 Band gap energy of $ZnIn_2S_4$, DC-g-C_3N_4.

Table S1 Comparison of AQE of ZIS3 with those of other catalysts reported in literature.

Entry	Catalysts	AQE (%)	Wavelength (nm)	ref
1	ZIS3	18.2	420	this work
2	CNB NS	7.45	420	[1]
3	MoS_2/CQDs/$ZnIn_2S_4$	25.6	420	[2]
4	Pt/$Ni(OH)_2$-C_3N_4	11.2	420	[3]
5	γ-TiO_2@ZIF-8	50.89	380	[4]
6	quasi-honeycomb g-C_3N_4	6.27	400	[5]
7	g-C_3N_4-M_1U_2	74.0	400	[6]
8	Pt/CNS	2.4	420	[7]
9	O substituted g-C_3N_4	13.2	420	[8]
10	MoS_2/$ZnIn_2S_4$	3.08	420	[9]
11	NiS/V-s-$ZnIn_2S_4$/WO_3	72.0	420	[10]
12	$ZnIn_2S_4$/$MoSe_2$	21.39	420	[11]

13	Co-P/$ZnIn_2S_4$	4.3	420	[12]
14	g-C_3N_4@$ZnIn_2S_4$	7.05	420	[13]
15	MoS_2/Cu-$ZnIn_2S_4$	13.6	420	[14]
16	Cu_3P-FCN	3.74	420	[15]
17	B/P-CNNs	3.24	420	[16]
18	CNAs	5.07	420	[17]
19	FeP/g-C_3N_4	1.57	420	[18]
20	g-C_3N_4/UMOFNs	2.34	405	[19]
21	3D CCNS-50	7.80	420	[20]
22	PtAu-2/g-C_3N_4	0.45	420±10	[21]
23	HC-CN	6.17	420	[22]
24	C-PAN/g-C_3N_4	5.60	420	[23]
25	g-C_3N_4 NS/TMC	4.10	420	[24]

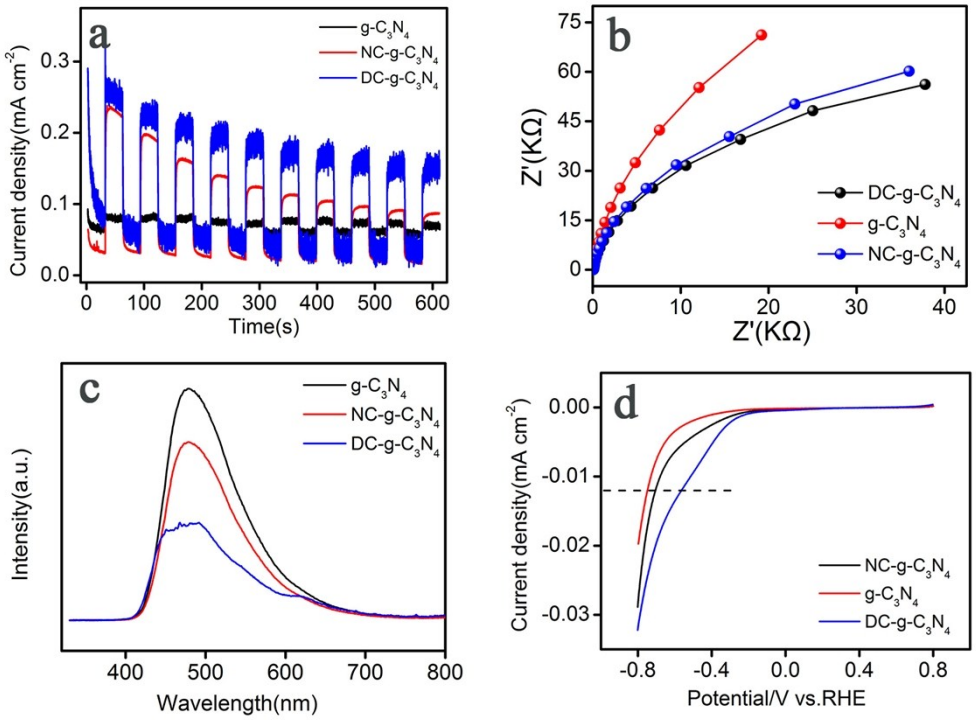

Fig. S7 Transient photocurrent–time (I–t) curves (a), electrochemical impedance spectroscopy (EIS) Nyquist plots of different samples in 0.2 M Na_2SO_4 solution (b), photoluminescence spectra (c) and linear sweep voltammetry (LSV) curves (d) of pristine g-C_3N_4, NC-g-C_3N_4 and DC-g-C_3N_4.

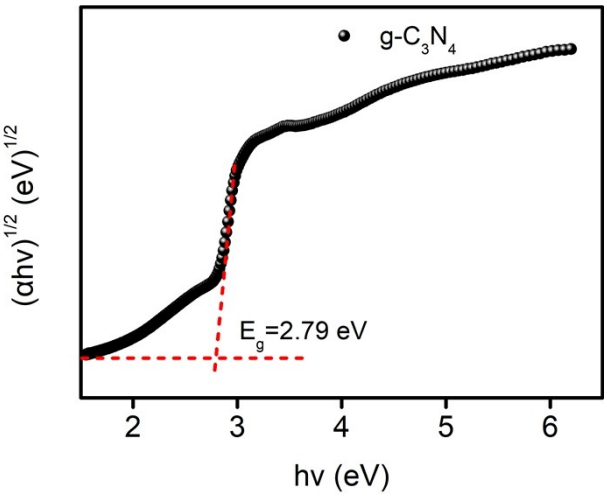

Fig. S8 Band gap energy of pristine g-C_3N_4.

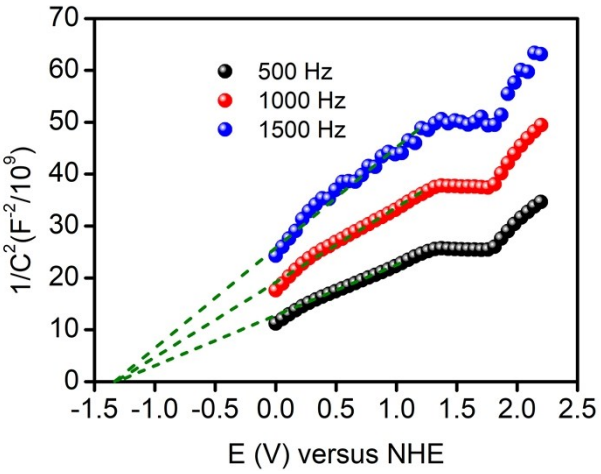

Fig. S9 Mott-Schottky plots of pristine g-C_3N_4.

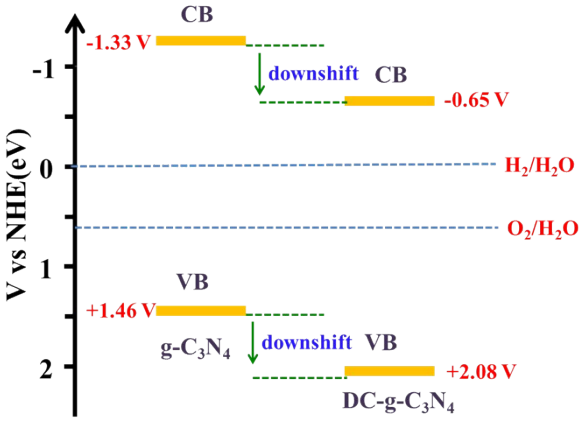

Fig. S10 Electronic structure of pristine g-C_3N_4 and DC-g-C_3N_4.

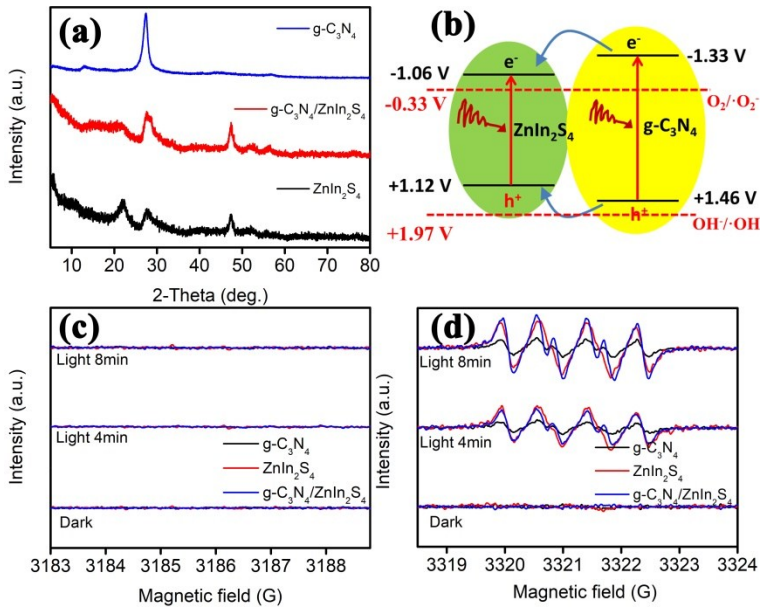

Fig. S11 XRD patterns of the as-prepared samples (a). Plausible charge transfer process between pristine g-C_3N_4 and $ZnIn_2S_4$ (b). •OH (c) and $•O_2^-$ (d) radical active species text by EPR over g-C_3N_4, $ZnIn_2S_4$ and g-C_3N_4/$ZnIn_2S_4$ photocatalysts using DMPO as radical adducts.

Pristine g-C_3N_4 and g-C_3N_4/$ZnIn_2S_4$ photocatalysts were also prepared in this work for comparison and the corresponding XRD patterns were given in Fig. S11a. On the basis of Mott-Schottky data, the conduction band and valence band edge potentials were determined to be -1.33 V and 1.46 V versus NHE, respectively. And the band edge alignment of pristine g-C_3N_4 and $ZnIn_2S_4$ were illustrated in Fig. 11b. Clearly, a straddling gap feature exists between g-C_3N_4 and $ZnIn_2S_4$. Hence, the photogenerated electrons and holes are likely to transfer to $ZnIn_2S_4$ from g-C_3N_4, forming a type-I structure. Furthermore, EPR analyses can give further evidence of the above supposition. As shown in Fig. 11c, it is seen that no obvious DMPO-•OH EPR signal was observed for all as-prepared samples. On the other hand, the EPR data of $•O_2^-$ (Fig. S11d) active species demonstrated that the reduction ability of photogenerated electrons for g-C_3N_4/$ZnIn_2S_4$ heterojunction had no obvious changed in comparison to

pristine g-C_3N_4 and $ZnIn_2S_4$, suggesting the formation of type-I structure between $ZnIn_2S_4$ and g-C_3N_4 without defects.

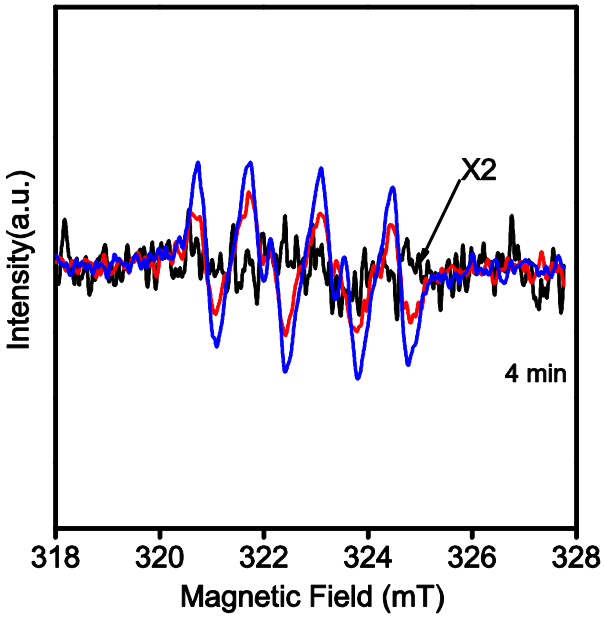

Fig. S12 EPR spectra of DC-g-C_3N_4, $ZnIn_2S_4$ and ZIS3 using DMPO as radical adducts for trapping $\bullet O_2^-$ species under visible light irradiation. The enlarge EPR signal represents DC-g-C_3N_4.

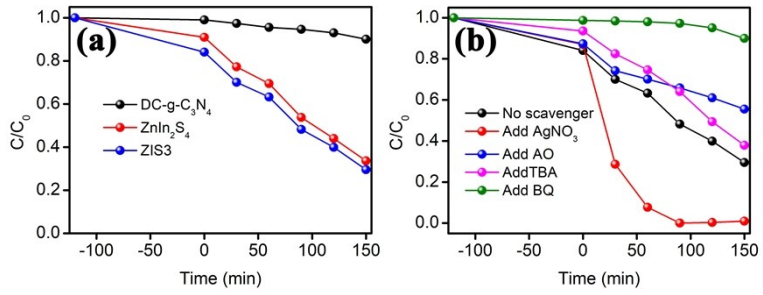

Fig. S13 Photocatalytic methyl orange (MO) degradation activity of DC-g-C_3N_4, $ZnIn_2S_4$ and ZIS3 (a). Effects of different scavengers on methyl orange degradation in the presence of ZIS3 under visible light irradiation (b).

Photocatalytic methyl orange degradation was selected as the model reaction aiming to investigate the photooxidation ability of the obtained samples. Fig. S13a declared that ZIS3 exhibited the higher degradation efficiency than their counterparts. And different scavengers were added in order to determine the primary radical species during the photocatalytic process, as displayed in Fig. S13b. Clearly, the photocatalytic performance of ZIS3 was apparently inhibited with the addition of ammonium oxalate (AO), tert-butyl alcohol (TBA) and benzoquinone (BQ) as hole (h^+), hydroxyl radical (•OH) and superoxide radicals (•O_2^-) scavenger, respectively. Meanwhile, the photocatalytic degradation efficiency was greatly enhanced with the addition of $AgNO_3$ because of the improvement of the separation efficiency of photogenerated carriers after Ag reduction. According to previous reports, hydroxyl radical (•OH) and superoxide radicals (•O_2^-) exhibited strong oxidation ability which play important roles in photocatalytic reaction. Hence, the photo-degradation MO was dominated by the photogenerated holes and the subsequent generated •O_2^- and •OH.

Reference

[1] W. Xing, G. Chen, C. Li, Z. Han, Y. Hu, Q. Meng, Doping effect of non-metal group in porous ultrathin g-C_3N_4 nanosheets towards synergistically improved photocatalytic hydrogen evolution, Nanoscale 10 (2018) 5239-5245.

[2] B. Wang, Z. Deng, X. Fu, Z. Li, MoS_2/CQDs obtained by photoreduction for assembly of a ternary MoS_2/CQDs/$ZnIn_2S_4$ nanocomposite for efficient photocatalytic hydrogen evolution under visible light, J. Mater. Chem. A 6 (2018) 19735-19742.

[3] S. Sun, Y. Zhang, G. Shen, Y. Wang, X. Liu, Z. Duan, L. Pan, X. Zhang, J. Zou, Photoinduced composite of Pt decorated $Ni(OH)_2$ as strongly synergetic cocatalyst to boost H_2O activation for photocatalytic overall water splitting, Appl. Catal. B: Environmental 243 (2019) 253-261.

[4] M. Zhang, Q. Shang, Y. Wan, Q. Cheng, G. Liao, Z. Pan, Self-template synthesis of double-shell TiO_2@ZIF-8 hollow nanospheres via sonocrystallization with enhanced photocatalytic activities in hydrogen generation, Appl. Catal. B: Environmental 241 (2019) 149-158.

[5] R. Cao, H. Yang, X. Deng, P. Sun, S. Zhang, X. Xu, Construction of 3DOM carbon nitrides with quasi-honeycomb structures for efficient photocatalytic H_2 production, ChemCatChem 10 (2018) 5656-5664.

[6] D. Ruan, S. Kim, M. Fujitsuka, T. Majima, Defects rich g-C_3N_4 with mesoporous

structure for efficient photocatalytic H_2 production under visible light irradiation, Appl. Catal. B: Environmental 238 (2018) 638-646.

[7] M. Liu, P. Xia, L. Zhang, B. Cheng, J. Yu, Enhanced photocatalytic H_2-production activity of g-C_3N_4 nanosheets via optimal photodeposition of Pt as cocatalyst, ACS Sustain. Chem. Eng. 6 (2018) 10472-10480.

[8] C. Liu, H. Huang, W. Cui, F. Dong, Y. Zhang, Band structure engineering and efficient charge transport in oxygen substituted g-C_3N_4 for superior photocatalytic hydrogen evolution, Appl. Catal. B: Environmental 230 (2018) 115-124.

[9] C. Liu, B. Chai, C. Wang, J. Yan, Z. Ren, Solvothermal fabrication of MoS_2 anchored on $ZnIn_2S_4$ microspheres with boosted photocatalytic hydrogen evolution activity, Int. J. Hydrogen Energy 43 (2018) 6977-6986.

[10] Z. Li, J. Hou, B. Zhang, S. Cao, Y. Wu, Z. Gao, X. Nie, L. Sun, Two-dimensional Janus heterostructures for superior Z-scheme photocatalytic water splitting, Nano Energy 59 (2019) 537-544.

[11] D. Zeng, L. Xiao, W. Ong, P. Wu, H. Zheng, Y. Chen, D. Peng, Hierarchical $ZnIn_2S_4/MoSe_2$ nanoarchitectures for efficient noble-metal-free photocatalytic hydrogen evolution under visible light, ChemSusChem 10 (2017) 4624-4631.

[12] Q. Liu, M. Wang, Y. He, X. Wang, W. Su, Photochemical route for synthesizing Co-P alloy decorated $ZnIn_2S_4$ with enhanced photocatalytic H_2 production activity

under visible light irradiation, Nanoscale 10 (2018) 19100-19106.

[13] B. Lin, H. Li, H. An, W. Hao, J. Wei, Y. Dai, C. Ma, G. Yang, Preparation of 2D/2D g-C_3N_4 nanosheet@$ZnIn_2S_4$ nanoleaf heterojunctions with well-designed high-speed charge transfer nanochannels towards high-efficiency photocatalytic hydrogen evolution, Appl. Catal. B: Environmental 220 (2018) 542-552.

[14] Y. Yuan, D. Chen, J. Zhong, L. Yang, J. Wang, M. Liu, W. Tu, Z. Yu, Z. Zou, Interface engineering of a noble-metal-free 2D-2D MoS_2/Cu-$ZnIn_2S_4$ photocatalyst for enhanced photocatalytic H_2 production, J. Mater. Chem. A 5 (2017) 15771-15779.

[15] W. Wang, X. Zhao, Y. Cao, Z. Yan, R. Zhu, Y. Tao, X. Chen, D. Zhang, G. Li, D. Phillips, Copper phosphide-enhanced lower charge trapping occurrence in graphitic-C_3N_4 for efficient noble-metal-free photocatalytic H_2 evolution, ACS Appl. Mater. Inter. (2019).

[16] B. Li, Y. Si, B. Zhou, Q. Fang, Y. Li, W. Huang, W. Hu, A. Pan, X. Fan, G. Huang, Doping-induced hydrogen-bond engineering in polymeric carbon nitride to significantly boost the photocatalytic H_2 evolution performance, ACS Appl. Mater. Inter. (2019).

[17] B. Lin, G. Yang, L. Wang, Stacking-layer-number dependence of water Adsorption in 3D ordered close-packed g-C_3N_4 nanosphere arrays for photocatalytic hydrogen evolution, Angew. Chem. Int. Ed. 58 (2019) 4587-4591.

[18] D. Zeng, T. Zhou, W. Ong, M. Wu, X. Duan, W. Xu, Y. Chen, Y. Zhu, D. Peng, Sub-5 nm ultra-fine FeP nanodots as efficient co-catalysts modified porous g-C_3N_4 for precious-metal-free photocatalytic hydrogen evolution under visible light, ACS Appl. Mater. Inter. 11 (2019) 5651-5660.

[19] Y. Liang, R. Shang, J. Lu, W. An, J. Hu, L. Liu, W. Cui, 2D MOFs enriched g-C_3N_4 nanosheets for highly efficient charge separation and photocatalytic hydrogen evolution from water, Int. J. Hydrogen Energy 44 (2019) 2797-2810.

[20] H. Gao, R. Cao, S. Zhang, H. Yang, X. Xu, Three-dimensional hierarchical g-C_3N_4 architectures assembled by ultrathin self-doped nanosheets: extremely facile hexamethylenetetramine activation and superior photocatalytic hydrogen evolution, ACS Appl. Mater. Inter. 11 (2019) 2050-2059.

[21] K. Bhunia, M. Chandra, S. Khilari, D. Pradhan, Bimetallic PtAu alloy nanoparticles-integrated g-C_3N_4 hybrid as an efficient photocatalyst for water-to-hydrogen conversion, ACS Appl. Mater. Inter. 11 (2019) 478-488.

[22] W. Xing, W. Tu, Z. Han, Y. Hu, Q. Meng, G. Chen, Template-induced high-crystalline g-C_3N_4 nanosheets for enhanced photocatalytic H_2 Evolution, ACS Energy Lett. 3 (2018) 514-519.

[23] F. He, G. Chen, J. Miao, Z. Wang, D. Su, S. Liu, W. Cai, L. Zhang, S. Hao, B. Liu, Sulfur-mediated Self-templating synthesis of tapered C-PAN/g-C_3N_4 composite

nanotubes toward efficient photocatalytic H_2 evolution, ACS Energy Lett. 1 (2016) 969-975.

[24] O. Elbanna, M. Fujitsuka, T. Majima, g-C_3N_4/TiO_2 mesocrystals composite for H_2 evolution under visible-light irradiation and its charge carrier dynamics, ACS Appl. Mater. Inter. 9 (2017) 34844-34854.